Surface & Coatings Technology 471 (2023) 129886

Contents lists available at ScienceDirect

Surface & Coatings Technology

journal homepage: www.elsevier.com/locate/surfcoat

Accelerated biodegradation of FeMn porous alloy coated with ZnO: Effect on cytocompatibility and antibiofilm properties

Aleksandra Bartkowska [a,1], Adam Benedict Turner [b,c,1], Andreu Blanquer [d,*], Aliona Nicolenco [e], Margarita Trobos [b,c,*], Carme Nogues [d], Eva Pellicer [a,**], Jordi Sort [a,f]

[a] Departament de Física, Universitat Autònoma de Barcelona, E-08193 Cerdanyola del Vallès, Spain
[b] Department of Biomaterials, Institute of Clinical Sciences, Sahlgrenska Academy, University of Gothenburg, Gothenburg, Sweden
[c] Centre for Antibiotic Resistance Research in Gothenburg (CARe), University of Gothenburg, Gothenburg, Sweden
[d] Departament de Biologia Cel·lular, Fisiologia i Immunologia, Universitat Autònoma de Barcelona, E-08193 Cerdanyola del Vallès, Spain
[e] CIDETEC Surface Engineering, Basque Research and Technology Alliance (BRTA), Paseo Miramon 196, 20014 Donostia-San Sebastian, Spain
[f] Institució Catalana de Recerca i Estudis Avançats (ICREA), Pg. Lluís Companys 23, E-08010 Barcelona, Spain

ARTICLE INFO

Keywords:
Zinc oxide coating
iron-manganese alloys
Biofilm
Cytocompatibility
Staphylococcus aureus
Saos-2

ABSTRACT

Fe-based alloys are being studied as potential candidates for biodegradable implants; however, their degradation rates remain too slow. To accelerate biodegradation while simultaneously hindering biofilm formation, a ZnO coating was deposited onto porous equiatomic FeMn alloy discs by sol-gel method using dip coating. The effect of the ZnO coating on the microstructure, biodegradability, cytocompatibility, and antibacterial properties were investigated. Biodegradability experiments were performed by immersing the specimens in Hank's balanced salt solution and measuring ion release after up to 28 days of immersion. The experiments showed an increased degradation of the FeMn/ZnO sample due to Fe segregation towards the grain boundaries, formation of iron-manganese oxide, and limited formation of degradation products on ZnO. Further, indirect Saos-2 cell cytotoxicity testing in 24 h sample-conditioned media showed no significant cytotoxicity in concentrations equal to or below 50 %. In addition, the total biofilm biovolume formed by *Staphylococcus aureus* on the FeMn/ZnO surface was significantly reduced compared to the uncoated FeMn. Taken together, these results show that the ZnO coating on FeMn improves the degradation rate, maintains cytocompatibility, and reduces biofilm accumulation when compared to an uncoated FeMn alloy.

1. Introduction

In recent years, metallic bioresorbable or biodegradable metals have emerged as potential candidates for stents and orthopaedic fixation devices such as bone pins, screws, wires, rods, or scaffolds [1–7]. The main idea behind biodegradable metals is to provide mechanical support while gradually degrading over a desired period of time and becoming completely dissolved when their function is fulfilled. Owing to the use of biodegradable materials, implant removal surgery can be avoided and thus the costs of medical treatment and risk of infection can be decreased [8,9]. Fe-based alloys are considered especially promising candidates for biodegradable implant applications due to their excellent mechanical properties and good biocompatibility. However, their degradation rate is rather slow, limiting their clinical applications [2,3,10,11]. Therefore, the scientific community is currently exploring various solutions to enhance the degradation rate of Fe-based alloys. The common approaches include alloying Fe with other elements (*e.g.*, C, Mn, Si), introducing porosity in the material, or macro-/nano-pattering [3,4,12–17]. In the past decade, surface modification approaches have emerged as an alternative and more efficient way to improve the overall performance of biodegradable metallic materials. These methods often involve ion implantation [18], laser ablation [19] or deposition of coatings [5,20–22]. For instance, zinc ion implantation on the surface of pure iron was found to accelerate the degradation rate by creating galvanic pairs between Fe and Zn clusters [18]. Modification of the Fe-Mn alloys surface by laser ablation increased their biodegradability

* Corresponding authors.
** Correspondence to: E. Pellicer, Departament de Física, Universitat Autònoma de Barcelona, E-08193 Cerdanyola del Vallès, Spain.
E-mail addresses: andreu.blanquer@uab.cat (A. Blanquer), margarita.trobos@biomaterials.gu.se (M. Trobos), eva.pellicer@uab.cat (E. Pellicer).
[1] A. Bartkowska and A.B. Turner contributed equally to this work as first authors.

https://doi.org/10.1016/j.surfcoat.2023.129886
Received 8 June 2023; Received in revised form 1 August 2023; Accepted 2 August 2023
Available online 4 August 2023

thanks to the formation of nanostructured metal oxides [19]. The deposition of coatings offers greater opportunities to adjust the corrosion and other characteristics of the system because the ultimate properties will arise from the interplay between the two components (bulk material and coating).

Recently, several authors have published reports on the improved properties of Fe-based alloys achieved by the deposition of second-phase coatings. For instance, Qi et al. [22] reported the mechanism of acceleration of Fe corrosion by polylactic acid (PLA) coating. A decrease in the local pH due to PLA hydrolysis and the fact that the PLA coating hindered the formation of a passivation layer were behind the observed enhanced degradation. In another report, polyethylene glycol (PEG) coatings were deposited on Fe alloy foam which helped improve its corrosion rate [20,21]. In a study by Huang et al. [23], a collagen coating was applied to the Fe-Mn alloy, and although it did not increase the corrosion rate of the alloy, it helped reduce cytotoxicity and improve osseointegration.

As biomaterial-associated infections are of concern, several approaches have been investigated to decrease the risk of infection [24,25]. One possible solution is the deposition of antibacterial and antibiofilm coatings on the biomaterial surface [26–28]. ZnO has been studied as an antibacterial material, demonstrating its capability to inhibit the growth of *Escherichia coli* [27] and *Staphylococcus aureus* [29,30]. The mechanism of antibacterial activity of ZnO is not yet well understood, but the production of reactive oxygen species on the surface of ZnO that cause oxidative stress to bacterial cells, ultimately causing their death is one of the plausible explanations [31]. Thin ZnO films can be deposited using a wide range of techniques such as sol-gel, spin- and dip-coating, metal-organic chemical vapour deposition, molecular beam epitaxy, pulsed laser deposition, or atomic layer deposition, amongst others [27,32,33]. Sol-gel approaches are especially attractive for their simplicity and ease of tailoring the properties of the synthesised films [33–35]. Several parameters of the sol-gel process can be controlled, such as the type of precursor and its concentration, the type of solvent and additives, the aging time of the mixture, the method of coating the substrate and post-heat treatment of the materials. Sol-gel-derived ZnO coatings have been successfully deposited on degradable Mg alloys [36] to increase cytocompatibility and osseointegration and inhibit bacterial adhesion and growth.

An implanted biodegradable material must be biocompatible (*i.e.*, it must show an appropriate host response upon implantation), it cannot cause a toxic or allergic inflammatory response or be thrombogenic. The biocompatibility of implant materials can be determined by two key factors – the host reaction (caused by implanted material) and the degradation of the material *in vivo* [37]. When studying degradable metals, the second factor is crucial. The abundant degradation products should not cause any inflammatory response. Enhanced biodegradability can influence cell viability and proliferation since the released corrosion products can lead to histological changes in local tissues, due to toxic solutes and also to hypersensitivity to allergens [38].

The objective of this work was to study the effect of ZnO sol-gel-derived coatings deposited on degradable porous FeMn alloys in terms of material biodegradability, cytocompatibility and microbial interactions. The purpose of the ZnO layer deposited on the FeMn alloy is two-fold: to favour the degradation of the alloy, and to confer antibiofilm properties to the material, without compromising its cytocompatibility.

2. Materials and methods

2.1. Synthesis and characterization of ZnO coating deposited on FeMn alloy

ZnO was deposited on FeMn porous alloy discs by dip-coating. The porous equiatomic FeMn alloys were fabricated by powder metallurgy, namely by ball milling of initial Fe and Mn powders, followed by pressing and sintering under vacuum at 900 °C. Details regarding the synthesis of the FeMn discs can be found elsewhere [15]. The ZnO precursor solution was prepared by mixing zinc acetate dihydrate ($Zn(CH_3COO)_2{\cdot}2H_2O$ > 99.0 % purity, Merck, Germany) as a starting material, ethanol as a solvent, and monoethanolamine (C_2H_7NO, MEA, >99 % purity, Merck, Germany) as a stabilizer. Zinc acetate and MEA were purchased from Merck and used without further purification. To a solution of 0.5 M zinc acetate, MEA was added, keeping the zinc acetate to MEA ratio of 1:1. The solution was stirred for 2 h at 60 °C using a magnetic stirrer working at 500 rpm to prepare a clear, homogenous solution, and then aged for 24 h at room temperature. Before deposition, the FeMn samples in the form of a flat disc with a diameter of 9 mm and thickness of 2 mm were polished up to #800 grit, ultrasonically cleaned in ethanol and dried using a nitrogen gun.

The ZnO precursor solution was deposited by dip-coating onto FeMn discs at a withdrawal rate of 300 mm/min using a Coater 5 AC (id Lab) operating at room temperature and 50 % relative humidity. To increase the thickness of the ZnO layers and improve surface coverage, the dipping process was repeated two times followed by mild annealing of the deposited layers at 120 °C for 20 min after each cycle. Finally, the coated FeMn substrates were annealed at 500 °C for 3 h in air using a Carbolite furnace. Uncoated FeMn discs were annealed under the same conditions and used as a reference for the ion release study.

The FeMn/ZnO samples were characterized using a scanning electron microscope (SEM, Zeiss Merlin, Zeiss, Germany) coupled with energy-dispersive X-ray spectroscopy (EDS) detector, operating at 5–20 kV. The thickness of the ZnO coating was assessed from SEM images of the discs tilted 60° towards the detector. The phase composition was investigated using grazing incidence X-ray diffractometer (GIXRD) and standard X-ray diffraction (XRD) analyses. The GIXRD patterns were acquired at room temperature using a Malvern Panalytical diffractometer operating at an angular 2Θ range of 25°–75°, with a step size of 0.02° and a counting time of 8 s. Standard XRD patterns were performed on a Panalytical X'Pert diffractometer (Malvern Panalytical, UK) with Cu Kα radiation, using an angular range of 20°–100°, with a step size of 0.026°.

2.2. Biodegradability test

The biodegradability of FeMn and FeMn/ZnO was studied under static immersion of the samples in Hank's balanced salt solution (HBSS, H8264, Merck, Germany) according to the ASTM-G31–72 standard. Prior to the tests, the samples were cleaned and sterilised in ethanol. Each disc, with a surface area of 1.25 cm^2, was immersed in plastic containers filled with 30 mL of HBSS solution. The containers were then placed in a water bath and kept at a constant temperature of 37.5 °C. The discs were kept in HBSS for up to 28 days. After 1, 3, 7, 14 and 28 days, the solution was withdrawn, and the containers were refilled with fresh media. The concentration of ions released from the material (Fe, Mn and Zn ions) to the media was measured by inductively coupled plasma-optical emission spectroscopy (ICP-OES, Agilent 7900, Agilent, USA). Prior to analysis, the media was treated with HNO_3 to dissolve the solid corrosion products suspended in the solution. Five replicas of each sample were analysed, and the results are presented as an average ± standard error (SE).

The corrosion rate was estimated according to the release of Fe and Mn after 1 day of sample's immersion [39] (Eq. (1)):

$$C_R = \frac{C^*V}{S^*T} \quad (1)$$

where C_R is the corrosion rate given in $g/m^2/day$; C is the released ion concentration (g/L), V is the solution volume (L), S is the sample surface area (m^2), and T is the incubation time (days).

To evaluate the morphological and compositional changes of the samples undergoing biodegradation, additional discs were immersed in

the HBSS. After 3, 7, 14, and 28 days, the specimens were removed from HBSS, rinsed with distilled water, dried using compressed nitrogen, and kept in a desiccator until further examination. Analyses were performed both on the surface and the cross-section of the discs. Once removed from the HBSS, the specimens were not immersed again. The cross sections were prepared by embedding the samples in resin, grinding, and polishing with diamond paste up to 1 μm. Top-down and cross-section SEM observations and EDS determinations were carried out at 10 kV and 20 kV, respectively.

FeMn and FeMn/ZnO samples immersed for 14 and 28 days were also characterized using X-ray diffraction to identify the products formed on the surface. The experiments were carried out on a Bruker diffractometer using Cu Kα radiation. The 2Θ region was between 20^0 and 100^0 with a step size of 0.026^0. The peaks were identified using X'Pert Panalytical software.

2.3. Cell proliferation assays and cytotoxicity analyses

In vitro cell proliferation and cytotoxicity of FeMn and FeMn/ZnO samples were assessed using human osteosarcoma cells (Saos-2 cell line; ATCC HTB-85). The cells were maintained in Dulbecco's Modified Eagle's medium (DMEM; Gibco, Thermo Fisher Scientific, USA) supplemented with 10 % fetal bovine serum (FBS; Gibco) at a controlled temperature of 37 °C and 5 % CO_2.

Samples were ultrasonically cleaned with distilled water and ethanol and then sterilised with pure ethanol. To prepare the conditioned media, the samples were immersed in supplemented DMEM for 24 h under standard conditions. A ratio of 1.25 cm^2/mL was used, as recommended by the ISO 10993-5:2009 standard. After 24 h, the samples were removed, and the conditioned media were kept at 4 °C protected from light until use. Next, the conditioned media were diluted to obtain the extract at the following concentrations: 100 % (non-diluted), 50 %, 25 %, and 12.5 % for further analysis. In parallel, control media were prepared by incubating media for 24 h, without any sample to obtain aged media. ICP-OES was used to identify the released ion concentrations of Fe, Mn, and Zn ions in the concentrated conditioned media (100 % extract).

The metabolic activity of osteoblasts was determined using the Alamar Blue reagent (Thermo Fisher Scientific, USA) after 1 and 3 days in order to evaluate the proliferation of cells exposed to the conditioned media. A total amount of 5×10^4 osteoblasts were seeded in a 24-well plate using fresh media. After 24 h, the media was replaced with conditioned media at different concentrations (100 %, 50 %, 25 %, and 12.5 %), and the cells were incubated for another 24 h under standard conditions. The conditioned media was then replaced with fresh media containing 10 % Alamar Blue and incubated for 4 h. Afterwards, the supernatant was collected (day 1), and fluorescence was analysed at a wavelength of 585 nm after excitation at 560 nm using a Spark multimode microplate reader (Tecan, Mannedorf, Switzerland). The cells were then incubated with the same conditioned media previously used and kept in the incubator during the Alamar Blue assay. Cells were cultured for 72 h in this conditioned media and the Alamar Blue assay was repeated as previously described (day 3). Aged and fresh media were used as the controls. The experiments were performed in triplicates.

In parallel, the cytotoxicity of conditioned media was assessed in cells grown for 3 days using the live/dead viability/cytotoxicity kit for mammalian cells (Invitrogen, United States) according to the manufacturer's protocol. Images of randomly selected regions were obtained using an Olympus IX71 inverted microscope equipped with epifluorescence.

2.4. Assessment of S. aureus adhesion and viability

2.4.1. Staphylococcus aureus ATCC 25923 culture conditions

Staphylococcus aureus ATCC 25923 (American Type Culture Collection, Manassas, USA) was streaked from a −80 °C glycerol stock onto 5 % Horse Blood Columbia Agar (HBA; Media Department, Clinical Microbiology Laboratory, Sahlgrenska University Hospital, Sweden) followed by aerobic incubation at 37 °C overnight. After incubation, isolated single colonies were picked with a flocked nylon swab and inoculated into 4 mL Tryptic Soy Broth (TSB; Scharlau, Barcelona, Spain) to achieve an optical density (OD_{546}) of 0.13, equivalent to 10^8 CFU/mL. This suspension was then diluted 1:1000 in TSB to achieve a final working bacterial suspension (inoculum) of 10^5 CFU/mL. Prior to inoculation with bacterial suspension, discs were sterilised by dry heat sterilisation at 180 °C for 2 h.

2.4.2. Viability of S. aureus after 4 h or 24 h biofilm formation

Dry-heat sterilised FeMn/ZnO and control FeMn discs (9 mm diameter, 2 mm thickness) were added to wells of a 48-well plate, inoculated with 1 mL of 10^5 CFU/mL of the previously mentioned *S. aureus* ATCC 25923 working bacterial suspension, and incubated aerobically and statically at 37 °C for either 4 or 24 h.

After each time point, discs were carefully removed from the well plate, rinsed three times in sterile saline (0.9 %), and transferred to a 15 mL Falcon Tube containing 1 mL sterile saline (0.9 %). Discs were then sonicated (42 kHz) in a Branson 3510MT Ultrasonic Cleaner (Branson, Brookfield CT, USA) for 30 s, followed by vortexing for 1 min at 10000 rpm. Disaggregated biofilm cells were then ten-fold serially diluted in a combination of sterile saline (0.9 %) and Triton-X (0.1 %). These dilutions were plated on 5 % HBA plates and incubated at 37 °C overnight and the viable colony-forming units (CFU) were subsequently enumerated. Three independent biological experiments with duplicate samples were performed.

2.4.3. Confocal laser-scanning microscopy and quantitative image analysis of S. aureus biofilms

Dry-heat sterilised FeMn/ZnO and control FeMn discs were added to wells of a 48-well plate, inoculated with 1 mL of 10^5 CFU/mL of *S. aureus* ATCC 25923 inoculum, and incubated aerobically and statically at 37 °C for either 4 or 24 h. Upon completion of each time-point, discs were carefully removed from the well plate and rinsed 3 times in sterile saline (0.9 %). After which, *S. aureus* adhered to the surface were stained using FilmTracer LIVE/DEAD Biofilm Viability Kit (Invitrogen, Waltham, United States) in the dark at room temperature for 20 min. After staining, discs were rinsed in sterile saline (0.9 %) to remove unbound stain and transferred to a 35 mm petri-dish containing 3 mL sterile saline for imaging on a Nikon C2+ confocal laser-scanning microscope (CLSM; Nikon, Tokyo, Japan) with a 100× water-dipping objective (CFI Plan 100XC W). Images were taken with *Z*-slices of 3 μm through the *S. aureus* biofilms. Biofilm thickness and biovolume were measured using BiofilmQ [40]. Sections imaged were taken from five randomly selected fields of view on each material sample. Three independent biological experiments were performed with technical duplicates.

2.4.4. SEM imaging of S. aureus ATCC 25923

Dry-heat sterilised FeMn/ZnO and FeMn discs were added to wells of a 48-well plate, inoculated with 1 mL of 10^5 CFU/mL of *S. aureus* ATCC 25923, and incubated aerobically and statically at 37 °C for 24 h. After incubation, both the control FeMn and FeMn/ZnO samples were carefully removed from the well plate and rinsed 3 times in sterile saline (0.9 %). Following this, *S. aureus* adhered to the surface were fixed in 4 % formaldehyde (HistoLab AB, Sweden) for 1 h at room temperature before dehydration in a graded ethanol series (50-, 70-, 80-, 90-, 95-, 100 %), for 5 min at each concentration, with the final 100 % step being repeated once.

The discs and *S. aureus* biofilms adhered to the surface were gold sputtered (10 nm) using a Leica EM ACE600 Sputter Coater (Leica, Stockholm, Sweden) and imaged in secondary electron mode using an LEO 55 ULTRA FEG SEM (Zeiss, Germany) operating at 5 KV.

2.5. Statistical analysis

All quantitative data were analysed using GraphPad Prism 9 and biodegradability and cytocompatibility data is presented as the mean ± standard error of the mean. Statistical differences for biodegradability and cytocompatibility studies were obtained by one-way analysis of variance (ANOVA) with a Tukey correction. Microbiological data is presented as the mean ± standard deviation. Biofilm viability (CFU/mL) was analysed using an unpaired student's *t*-test. Differences in biofilm biovolume and thickness were analysed by paired Students *t*-test to compare between live and dead groups, and unpaired Students *t*-test for the comparisons between the two biomaterial groups. A value of $p < 0.05$ was considered significant.

3. Results

3.1. Morphology of the ZnO coating deposited on FeMn substrate

Fig. 1 displays the topography and morphology of the ZnO coating deposited on the FeMn substrate, together with the elemental distribution of Fe, Mn, Zn and O obtained by SEM + EDS. The porous FeMn substrate contains large pores, with a diameter of around 10 μm and nanopores, with a size around 100 nm, as presented in Fig. S1. The coating has a compact structure and is evenly distributed over the entire surface. However, Fig. 1A, B shows that the regions around the large pores have a distinct morphology. This was attributed to the difference in the wettability between the dense and porous areas of the sample. The regions around the pores were enriched in Mn, O, and Fe, with a very low Zn content, indicating the formation of iron-manganese mixed oxides. The ZnO coating formed a wrinkled network structure consisting of regions of higher thickness (*i.e.*, ganglia-like hills) with a thickness of approximately 2 μm, as well as flat regions with a thickness of approximately 600 nm, as shown in Fig. 1C, D. The flat areas of the ZnO coating possessed a mesoporous structure, as shown in Fig. 1E.

Similar morphologies of ZnO thin films have been previously described in the literature [32,34]. Several explanations have been put forward to explain the morphology of ZnO films, such as stress relaxation and slow cooling conditions. In our case, we attributed the wrinkled morphology to stress relaxation due to the difference in the thermal expansion coefficient between the metallic disc underneath and the thin film, as suggested by Kwon et al. [41]. The sol-gel methods make it possible to obtain a material using a sol or a gel as an intermediate step with the process being conducted at lower temperatures than traditional methods [33,35]. The sol-gel processes can be divided into the (i) preparation of precursor solution, (ii) sol deposition on the substrate by spin- or dip-coating and (iii) heat treatment of the xerogel film. During the drying process of sol-gel-derived films, when the solvent is removed, compressive stress is generated in the system owing to the difference in the thermal expansion coefficients between the film and the substrate. This likely led to the formation of a wrinkled structure in the gelated ZnO film. In the samples described here, apart from the wrinkled ZnO coating, a layer of Fe-Mn oxide was also present, which was formed during the annealing process.

The GIXRD pattern of the dip-coated ZnO layer on the FeMn substrate is shown in Fig. 2. This pattern confirms the formation of polycrystalline ZnO in the hexagonal wurtzite phase (space group *P63mc*), as

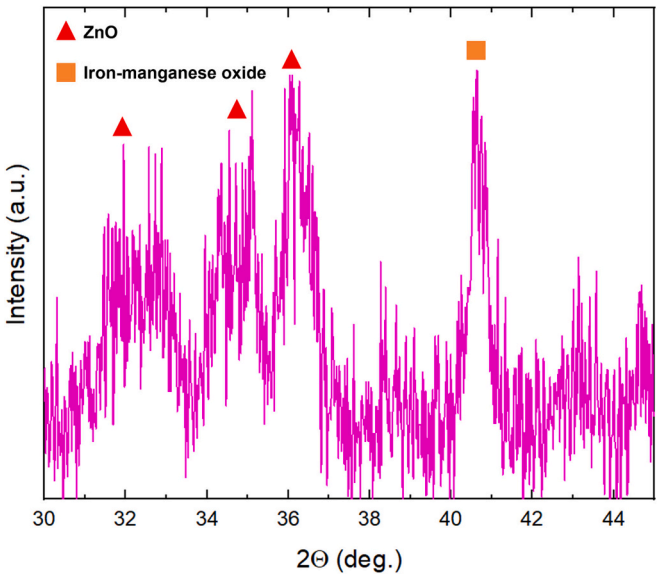

Fig. 2. GIXRD pattern of FeMn/ZnO sample. Triangles correspond to the ZnO hexagonal phase, while squares belong to the iron-manganese oxide phase formed during annealing.

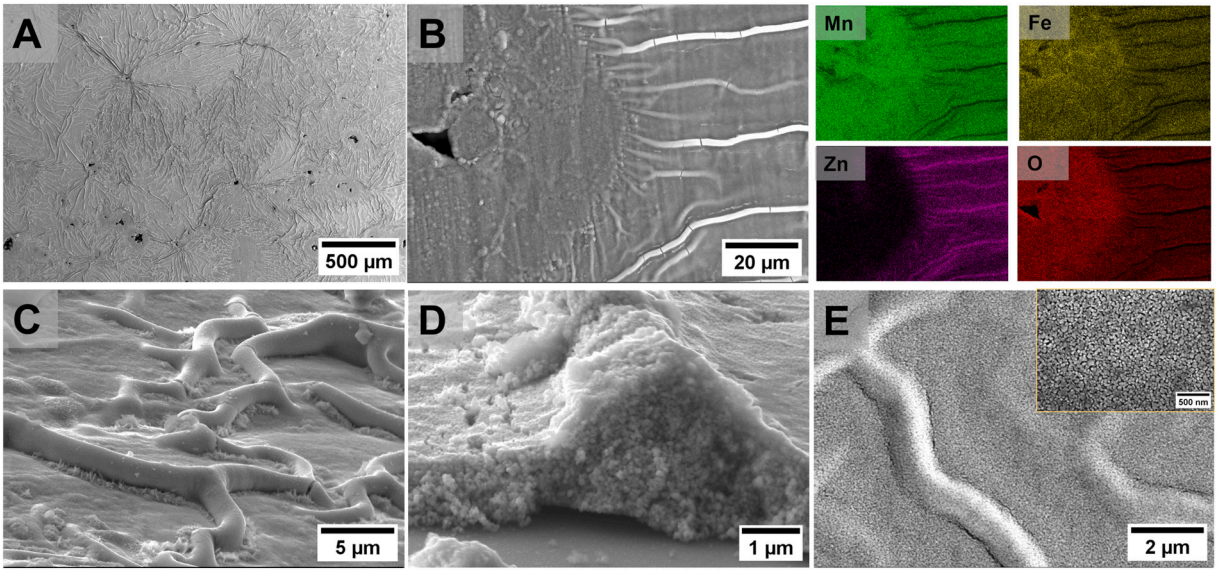

Fig. 1. Morphology of the ZnO film deposited on the FeMn substrate: (a) low-magnification view of the coating, (b) SEM image and EDX map of the area, (c) tilted view of coating' wrinkles, (d) magnified view of a wrinkle and (e) morphology of the coating at the flat areas, showing a detail of the mesoporosity in the inset.

evidenced by the presence of characteristics peaks for this phase at the 2Θ values of 31.9°, 34.4° and 36.3°, corresponding to (100), (002) and (101) planes, respectively. No preferred orientation was observed; therefore, we can conclude that the ZnO crystallites possess random orientation. Besides the ZnO phase, an additional peak was identified at 40.6^0, which is consistent with the (200) plane of iron manganese oxide phase with space group *Fm-3m*. The presence of this oxide is in accordance with the EDS mapping presented in Fig. 1.

3.2. Biodegradability of FeMn/ZnO

A first biodegradability test was conducted to assess the changes in the surface morphology and composition of the FeMn/ZnO samples and to measure ion release upon immersion in HBSS. The in-plane views after 3, 7, 14, and 28 days of incubation are presented in Fig. 3. The results of the EDS analysis obtained from the areas highlighted in Fig. 3 (black letters A–D, corresponding to FeMn and numbers 1–4, corresponding to FeMn/ZnO) are shown in Table 1.

The corrosion products formed on the uncoated FeMn alloy after 3, 7, and 14 days of immersion had a size of a few micrometres and mostly consisted of globular precipitates that were not uniformly distributed on the surface. These were identified as Ca, P, and Cl-containing precipitates by EDS. After immersion for 14 and 28 days, the amount of Ca and P precipitates formed on the surface of the FeMn alloys appeared much higher than for the FeMn/ZnO samples (Table 1). After 28 days of immersion, a compact corrosion layer was formed, covering the entire surface. This compact corrosion layer can act as a protective barrier, hindering the progression of corrosion.

The morphologies of the corrosion products formed on the surface of the FeMn/ZnO samples showed different features. Following immersion for a maximum of 14 days, the distinctive morphology of the ZnO coating can be still observed, indicating that it had not been entirely engulfed by corrosion products. The products primarily consist of loosely packed globular precipitates, identified as Ca, P and Cl precipitates. However, following a 28-day immersion period, a denser layer of corrosion products accumulated on the surface of the ZnO coating. This layer included some platelet-like structures that have been recognized as Ca-P apatite-like precipitates [4,14]. The formation of these precipitates is *a priori* positive, since it increases the bioactivity of the surface, eventually leading to a better bone-bonding ability of the material [42].

The XRD patterns of FeMn and FeMn/ZnO samples in the as-prepared state and after 14 and 28 days of degradation in HBSS are displayed in Fig. 4A, B. FeMn specimens (Fig. 4A) in the as-prepared state and after 14 days of immersion in HBSS show the same phase composition (γ-austenite and Fe-Mn oxide phases), while after 28 days of immersion, new peaks matching the $MnCO_3$ phase appear. Indeed, the formation of corrosion products such as carbonates and phosphates resulting from the reaction between samples and the surrounding HBSS environment is common [9]. The HBSS contains HCO_3^- and HPO_4^- ions which may react with the released metallic ions, thus forming insoluble metal carbonates or phosphates. The latter deposit on the metallic surface, slowing down further degradation. In the case of the FeMn/ZnO sample (Fig. 4B), three characteristic peaks of ZnO, the γ-austenite phase, as well as the iron-manganese oxide phase (identified as well in Fig. 2), are present in all samples. Moreover, one can observe the presence of the α-Fe in the FeMn/ZnO samples, most probably due to the segregation of Fe on the grain boundaries after the annealing step required to convert the ZnO precursor into ZnO. No peaks ascribed to corrosion products are observed, which would agree with our previous observation that the ZnO might hinder the formation of corrosion products. Hence, the main difference between the uncoated and ZnO-coated discs resides in the phase composition of the FeMn substrate: austenite and ferrite phases coexist in the FeMn/ZnO sample, while the naked substrate has a purely austenitic structure. It is anticipated that the occurrence of the austenite and ferrite phases in the FeMn/ZnO samples might contribute to accelerating their degradation in bodily fluids [3,43].

In addition, having analysed Figs. 3 and 4, it is likely that the ZnO coating acts as a physical barrier in the initial stages of degradation, protecting the surface of FeMn alloy from direct contact with the corrosive environment, therefore, limiting the deposition of insoluble corrosion products from HBSS. In fact, the amounts of Ca- and P-containing products after 7 days of incubation are lower (Table 1). However, over time, the penetration of HBSS through the pores might allow for the initiation of localized corrosion. Moreover, as the ZnO coating is not fully dense, media can easily permeate through the defects and pores and cause micro galvanic corrosion between the semiconductor coating and the metallic substrate.

Fig. 5 shows the cumulative ion release of Fe (A) and Mn (B) in (uncoated) FeMn, annealed FeMn and FeMn/ZnO samples after 1, 3, 7, 14 and 28 days of immersion for both Fe and Mn release after 1 day (C) and 28 days (D) of immersion in HBSS. It can be observed that the release of both Fe and Mn increases over time, with significant differences between FeMn and FeMn/ZnO samples. The release of Fe and Mn ions in FeMn/ZnO samples after 1 day was 5.50 ± 0.94 ppm and 9.00 ± 0.86 ppm, respectively. In uncoated FeMn the release after 1 day in HBSS was much lower and reached 0.06 ± 0.02 ppm for Fe ions and 0.33 ± 0.04 ppm for Mn ions (Fig. 5A). Note that the release of Fe and Mn ions after 1 day is significantly different for FeMn/ZnO sample, while both ions are released in similar amounts from the uncoated FeMn sample. The release after 28 days in HBSS for FeMn/ZnO reached the value of

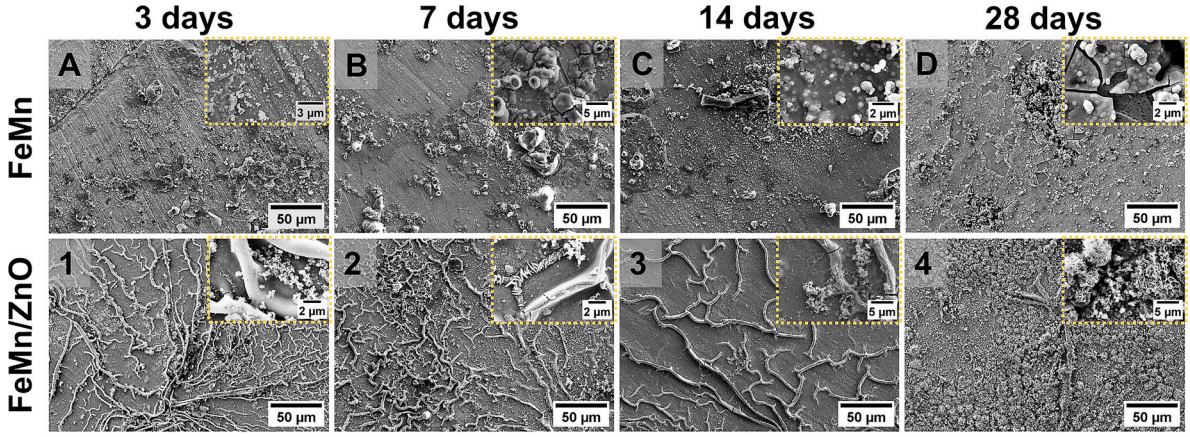

Fig. 3. Top-down SEM micrographs of the surface of FeMn and FeMn/ZnO samples after 3, 7, 14 and 28 days of immersion in HBSS at 37.5 °C. Black letters A–D correspond to FeMn, and numbers 1–4 correspond to FeMn/ZnO immersed for 3, 7, 14, and 28 days, respectively.

Table 1
EDS analysis of the areas presented in Fig. 3. A, B, C, and D correspond to areas of FeMn samples immersed for 3, 7, 14, and 28 days, respectively. Meanwhile, 1, 2, 3, and 4 correspond to areas of FeMn/ZnO samples immersed for 3, 7, 14, and 28 days.

Sample	EDS analysis	Element (wt.%)							
		Fe	Mn	O	Zn	Ca	P	Cl	Mg
FeMn 3d	A	42.9 ± 5.0	35.4 ± 5.4	18.4 ± 2.0	X	X	X	3.3 ± 0.7	X
FeMn/ZnO 3d	1	4.2 ± 0.1	32.1 ± 0.2	19.8 ± 0.2	38.4 ± 0.2	2.6 ± 0.1	1.3 ± 0.1	1.2 ± 0.1	0.5 ± 0.1
FeMn 7d	B	41.9 ± 0.8	36.4 ± 0.8	16.4 ± 0.3	X	1.3 ± 0.1	X	4.1 ± 0.1	X
FeMn/ZnO 7d	2	12.6 ± 0.6	26.5 ± 0.8	25.6 ± 0.4	30.6 ± 0.4	1.4 ± 0.1	2.3 ± 0.1	0.9 ± 0.1	X
FeMn 14d	C	33.6 ± 0.7	31.2 ± 0.9	23.8 ± 0.4	X	2.9 ± 0.1	4.0 ± 0.1	4.6 ± 0.1	X
FeMn/ZnO 14d	3	1.8 ± 0.5	30.7 ± 0.6	22.3 ± 0.3	38.6 ± 0.4	0.7 ± 0.1	0.5 ± 0.1	0.8 ± 0.1	X
FeMn 28d	D	26.3 ± 0.7	29.7 ± 0.9	24.3 ± 0.4	X	9.7 ± 0.2	8.1 ± 0.2	0.9 ± 0.1	1.1 ± 0.1
FeMn/ZnO 28d	4	4.8 ± 0.1	36.1 ± 0.2	27.6 ± 0.2	17.5 ± 0.2	2.0 ± 0.1	3.1 ± 0.1	8.5 ± 0.1	0.3 ± 0.1

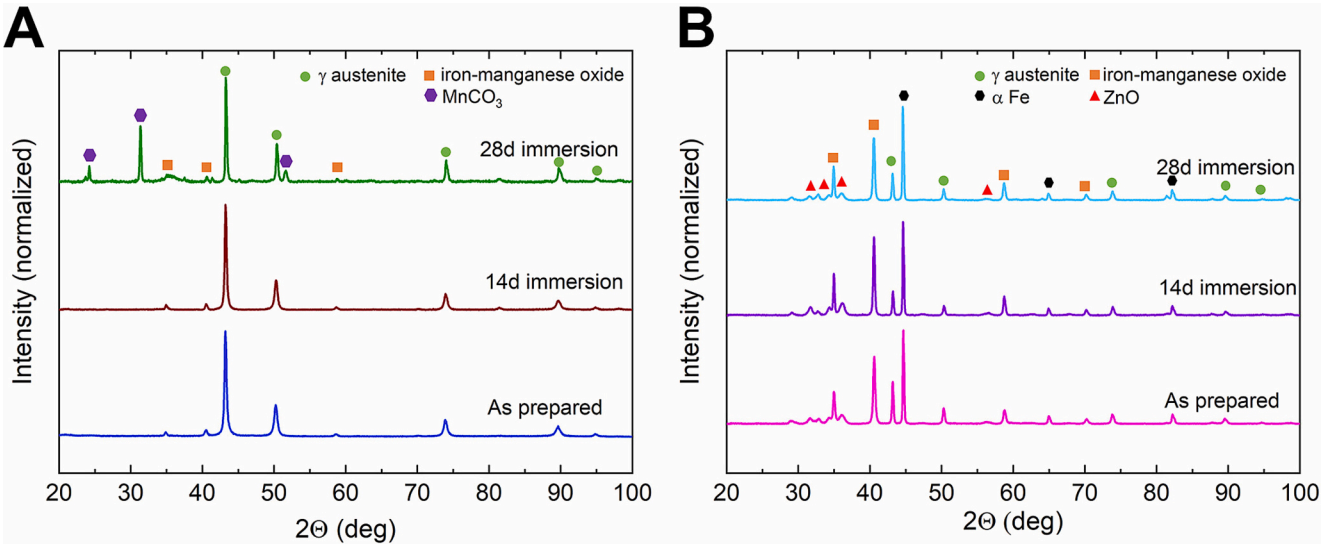

Fig. 4. X-ray diffraction patterns of the as-prepared and immersed for 14 and 28 days in HBSS samples of (A) FeMn and (B) FeMn/ZnO.

14.70 ± 1.55 ppm for Fe and 21.69 ± 1.38 ppm for Mn ions (again, significantly higher), while for FeMn it reached the value of 0.34 ± 0.05 ppm for Fe and 2.9 ± 0.29 ppm for Mn (Fig. 5B). In general, the release of Fe ions is lower than that of Mn. The concentration of Zn^{2+} ions in the FeMn/ZnO samples was very low, reaching only 0.15 ppm after 28 days of immersion (not shown).

As a reference, ion release from annealed (uncoated) FeMn discs was tested. An elevated ion release after 1 to 28 days of immersion was observed when compared to the uncoated, non-annealed FeMn disc (Fig. 5C, D). Yet, the release of Fe and Mn ions was lower than for the FeMn/ZnO sample. The release of Mn was also lower when compared to the FeMn/ZnO sample, but it reached the same concentration after 28 days of immersion.

Overall, the release of Fe after 28 days of immersion is 43 times higher (and the release of Mn 7.5 times higher) in FeMn/ZnO sample than in FeMn. The significant differences between FeMn, annealed FeMn and FeMn/ZnO samples indicate that the ZnO coating and the formation of secondary phases stemming from its synthesis would trigger the degradation of FeMn alloys in HBSS.

The concentration of metallic ions after 1 day of immersion in HBSS was used to make a rough estimation of the corrosion rates according to Eq. (1), and the results are shown in Fig. 6. A significant increase in the corrosion rate was observed for the FeMn/ZnO sample when compared to the uncoated FeMn alloy and the annealed (uncoated) FeMn samples. The corrosion rates of FeMn/ZnO were 36 times higher than that of FeMn and 3 times higher than that of annealed FeMn. This indicates that the enhanced degradability can be attributed to both Fe segregation due to annealing and the presence of the ZnO coating.

Fig. 7 presents the SEM images and linear EDS analysis of cross-sections of FeMn/ZnO discs in the as-prepared state and after 7, 14 and 28 days of immersion in HBSS. Linear EDS analysis was performed on these samples to identify the distribution of Fe, Mn, O, Zn and Ca on the cross-section of the samples. We can observe that already in the as-prepared state, there is a Mn- and O-enriched region, just below the ZnO coating, that can be recognized as the iron-manganese-rich oxide. Just below this layer we can observe a region enriched in Fe with reduced content of Mn, that, likewise, forms due to Mn diffusion towards the surface to form the aforementioned oxide layer. After 28 days we can observe that the Mn-rich region is becoming thicker upon degradation. The outermost layer contains Ca, coming from HBSS-derived precipitates.

Fig. 8 shows cross-section areas of the FeMn and FeMn/ZnO samples in the as-prepared state and after 7, 14 and 28 days of immersion in HBSS. Additional supplementary Fig. S2 presents the EDS mapping performed on the samples immersed for 28 days, where annealed FeMn sample was added as a reference as it has shown an ion release close to that of FeMn/ZnO. Uncoated FeMn and FeMn/ZnO samples present similar microstructural features after 7 days of immersion, with a degradation layer at the upper region. However, after 14 and 28 days of immersion, samples show distinct microstructures. The corrosion layer formed on the FeMn disc becomes thicker and more compact and the macropores are infilled with degradation products. Conversely, the FeMn/ZnO sample does not show a thick corrosion layer on the top surface. It does, however, show segregation of Fe around the pores, as highlighted by yellow arrows, and confirmed by EDS mapping in the supplementary information. Moreover, an increase in the size of the nanopores is observed in the denser region, highlighted by red arrows, which would indicate the dissolution of the FeMn matrix.

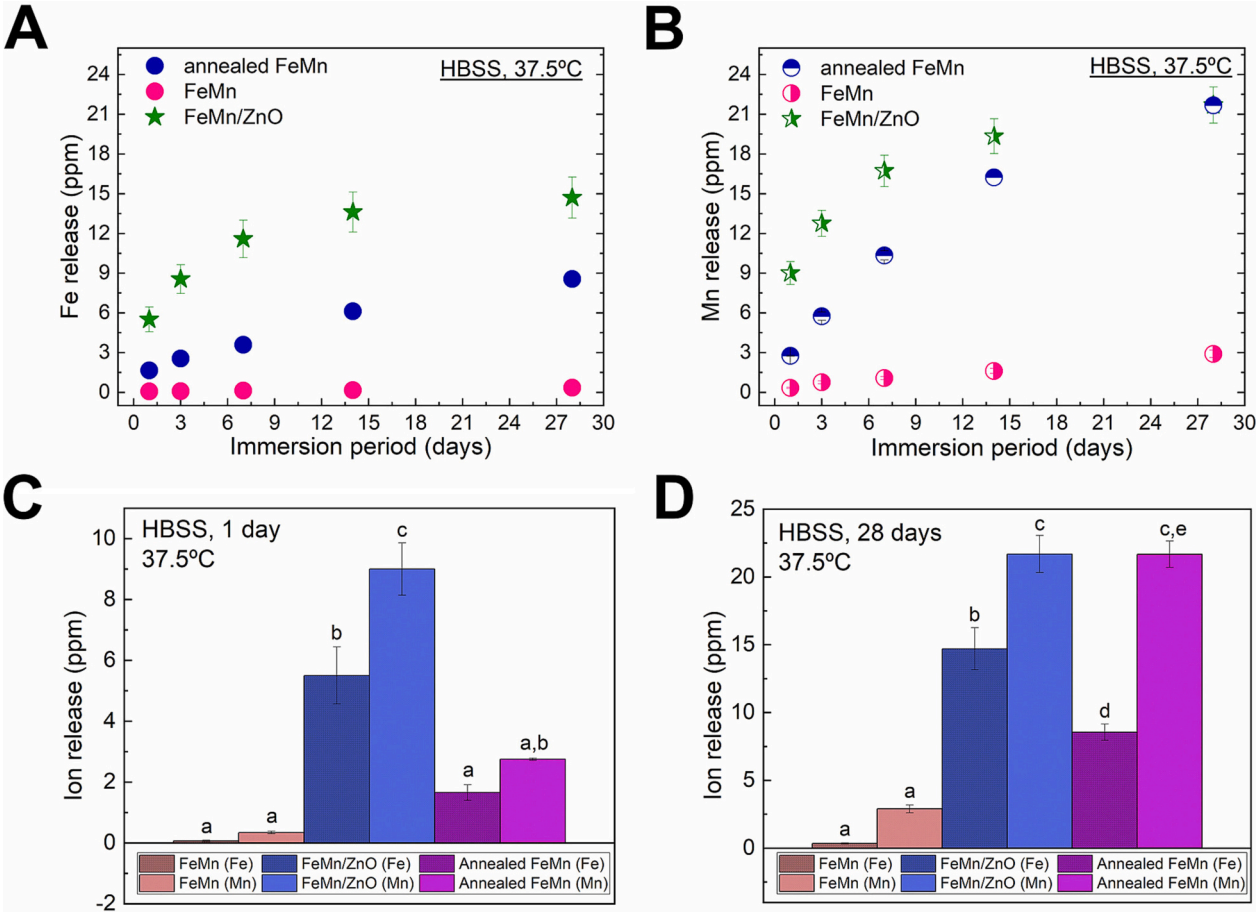

Fig. 5. Released ion concentration of Fe (A) and Mn (B) after 1, 3, 7, 14, and 28 days of immersion in HBSS for FeMn, annealed FeMn, and FeMn/ZnO samples. Analysis of significance for ion release after 1 (C) and 28 (D) days, comparing the release of Fe and Mn for the different samples. Bars marked with different alphabetical superscripts are significantly different from each other, while bars with the same superscript are not significantly different from each other.

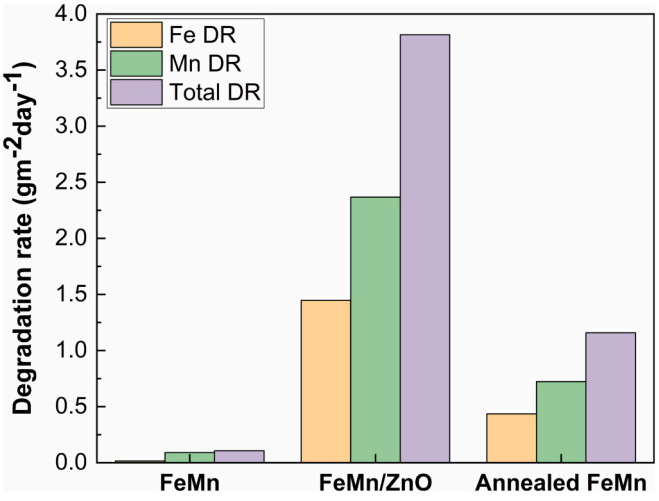

Fig. 6. Calculated corrosion rates of FeMn and FeMn/ZnO samples based on the released ion concentration after 1 day of immersion in HBSS calculated for both Fe and Mn ion release. The total corrosion rate is the sum of Fe and Mn corrosion rates for each sample. 'DR' stands for degradation rate.

3.3. *In vitro cytocompatibility and cell proliferation*

Cytocompatibility of the materials was assessed by cell proliferation and cytotoxicity using an indirect *in vitro* model on Saos-2 cells. The conditioned media used for the experiments were prepared at 100 %, 50 %, 25 % and 12.5 % concentrations. Similarly, the control media, conditioned for 1 day without any material, was also diluted with fresh media at previously mentioned concentrations.

Fig. 9A shows the ion release concentration after 1 day of incubation in DMEM for 100 % extract. The release of Fe ions was not significantly different for the two samples, whereas the release of Mn was significantly higher for the FeMn/ZnO sample. These results are in line with those previously observed for the ions leaching in HBSS (*cf.* Figs. 5C and 9A). The release of Zn ions (not shown in the plot) was 6.2 ± 0.7 ppm.

Regarding cell viability (Fig. 9B and C), the percentage of live cells was approximately 75 % for FeMn and 51 % for FeMn/ZnO using the conditioned medium at a concentration of 100 %, which was significantly lower than the control, FeMn and FeMn/ZnO conditioned media. However, the percentage of live cells was 90 % for both samples when the conditioned media was diluted to 50 and 12.5 %, without significant differences between both the samples and the concentrations. Results showed that with an increase in the dilution of the conditioned media, cell viability increased. The fluorescence microscopy images of the live/dead assay (Fig. 9B) for 12.5 % and 50 % conditioned medium showed a similar amount of live Saos-2 cells (green cells), with very few dead cells (red) for both samples. For the concentrated conditioned media (100 %), fewer cells were found for both samples compared to the control and diluted conditioned media. In addition, the conditioned media derived from FeMn/ZnO led to a higher ratio of dead cells than the FeMn sample.

The metabolic activity results after 1 and 3 days of incubation are presented in Fig. 9D–E and Supplementary Fig. S3. The fluorescence intensity of Alamar Blue (which corresponds to metabolic activity of the

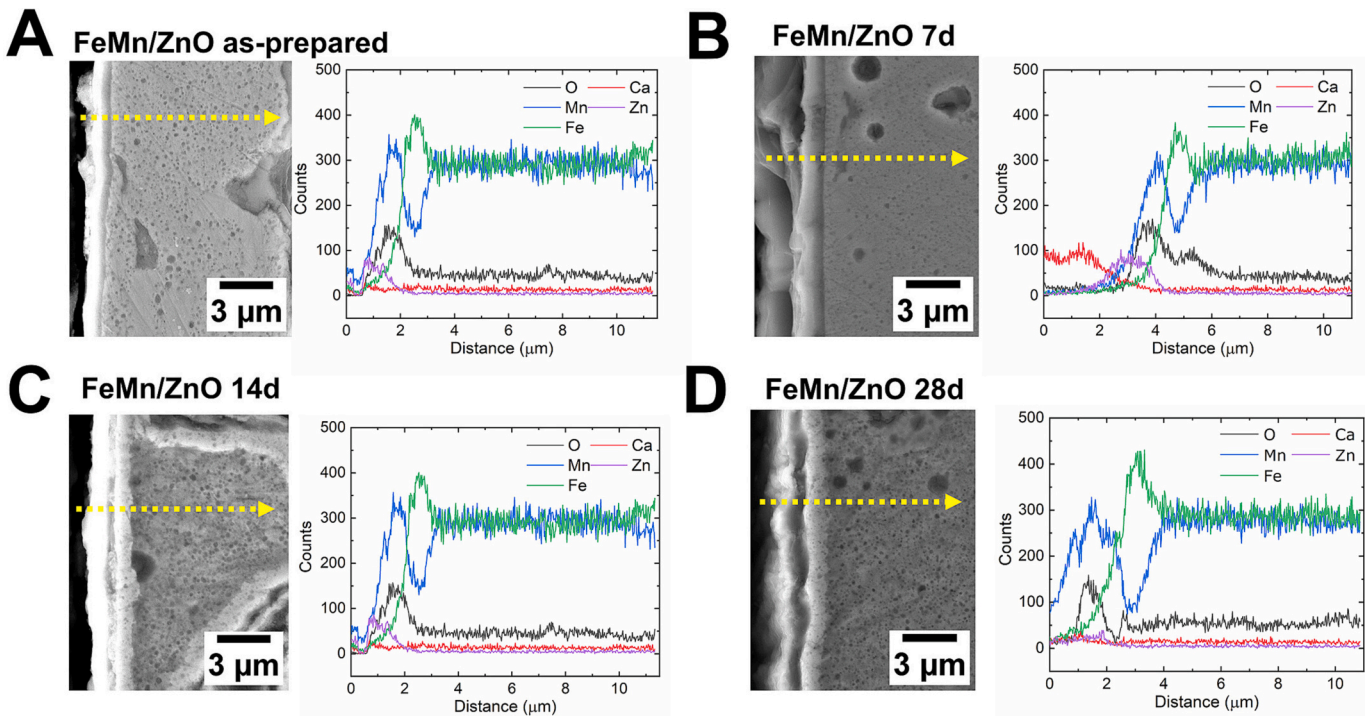

Fig. 7. EDS line scans for O, Mn, Fe, Ca and Zn elements along the cross-section of FeMn/ZnO samples in the as-prepared state (A) and after 7 (B), 14 (C), and 28 (D) days of immersion in HBSS. The yellow arrow indicates the direction of the EDS line scan. (For interpretation of the references to colour in this figure legend, the reader is referred to the web version of this article.)

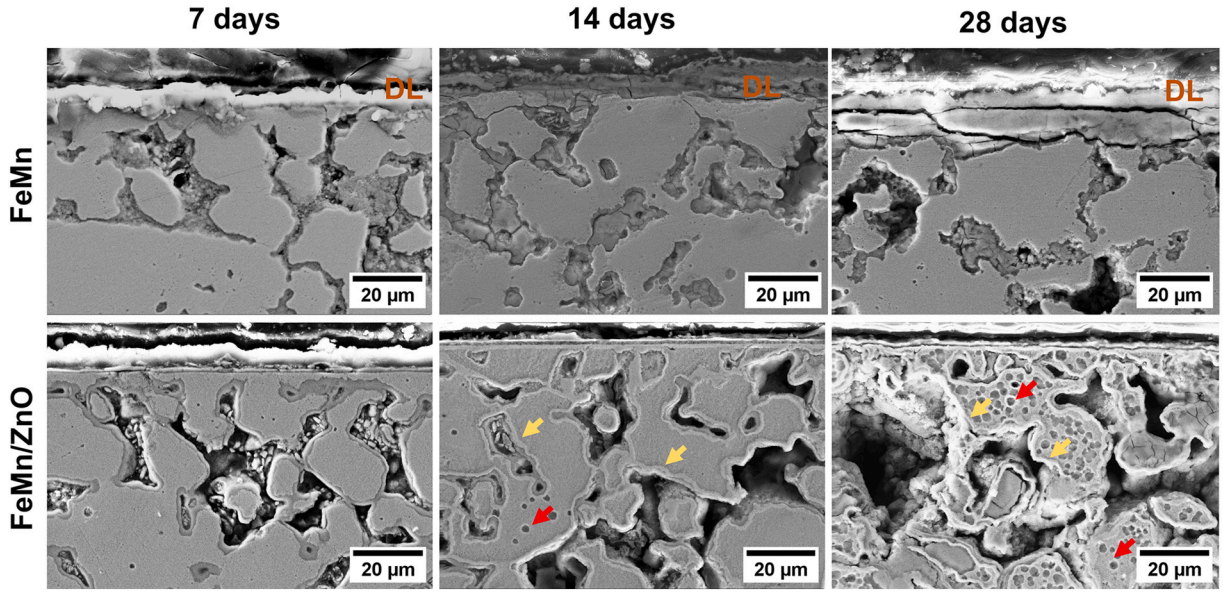

Fig. 8. Cross sections of FeMn and FeMn/ZnO samples immersed for 7, 14 and 28 days in HBSS. 'DL' stands for degradation layer formed on the surface. Yellow arrows indicate the Fe-enriched regions, while red arrows show increased pore size. (For interpretation of the references to colour in this figure legend, the reader is referred to the web version of this article.)

cells) increased with increasing dilution of the conditioned media, although no significant differences were observed amongst the 50 %, 25 % and 12.5 % dilutions. The 100 % concentrated conditioned media led to significant differences between the control, FeMn and FeMn/ZnO samples. A drastic change was observed when comparing the 100 % conditioned media with the diluted conditioned media for both materials in the sense that all materials (FeMn, FeMn/ZnO and control) showed similar metabolic activity. In supplementary Fig. S3, the differences in cell proliferation between days 1 and 3 of culture are presented. We observed that the metabolic activity in the 100 % conditioned media increased over time for the 24 h-control media, whereas it remained low and without significant differences between the FeMn and FeMn/ZnO samples. On the contrary, no significant differences were observed in cell proliferation between samples on day 1 of culture in the 50 % conditioned media, whereas significant differences arose after 3 days of culture between the 24 h-control media and FeMn conditioned media compared to day 1. The proliferation of the FeMn/ZnO sample after day 3 was not significantly different from that on day

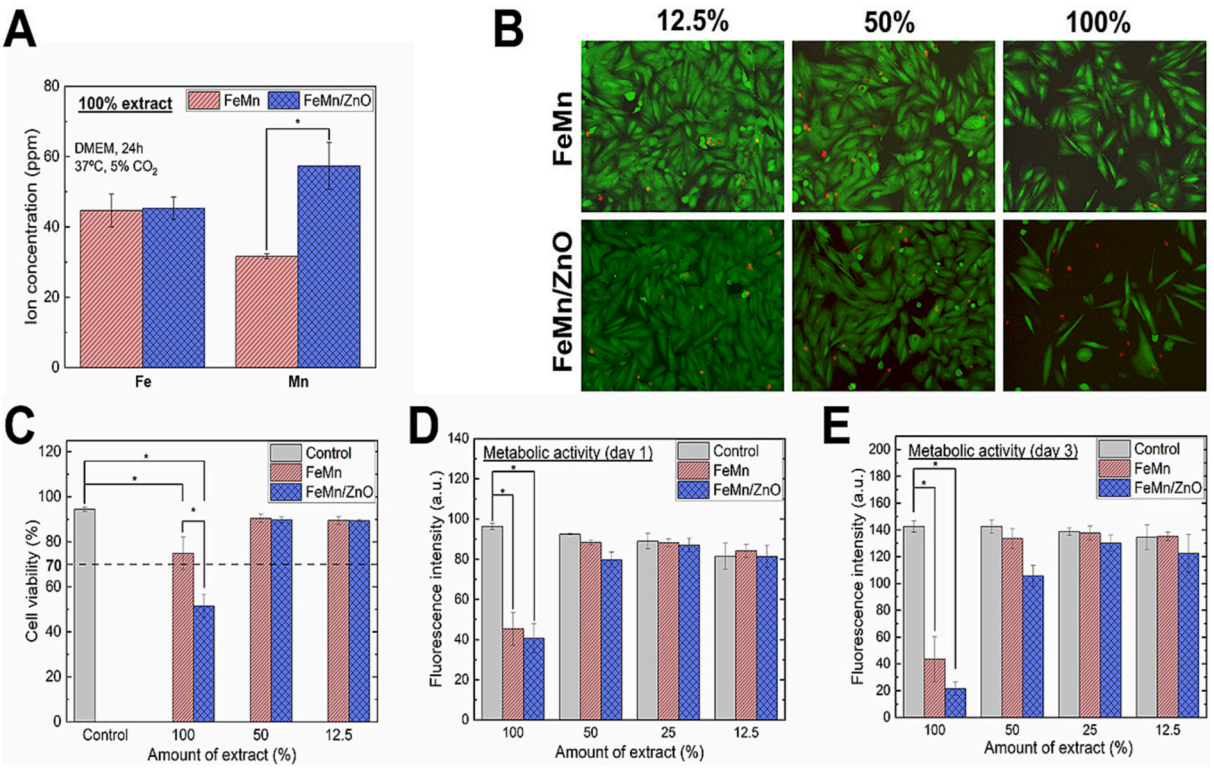

Fig. 9. Cytocompatibility assessment of FeMn and FeMn/ZnO samples obtained through indirect assay. The concentration of Fe and Mn ions released to the culture media after 24 h by FeMn and FeMn/ZnO samples (A), Live/Dead images of Saos-2 cells cultured indirectly in conditioned media from FeMn and FeMn/ZnO (B), the viability of Saos-2 cells cultured indirectly in conditioned media from FeMn and FeMn/ZnO (C). Metabolic activity of Saos-2 cells cultured in diluted conditioned media from FeMn and FeMn/ZnO samples after 1 day (D) and 3 days (E). Media conditioned for 1 day without any material was used as a control and diluted with fresh media. Significant differences are marked with (*). (For interpretation of the references to color in this figure, the reader is referred to the web version of this article.)

1.

3.4. Biofilm formation

In this study, the uncoated FeMn substrate was used as a control. *S. aureus* ATCC 25923 was incubated with and directly exposed to the control FeMn and the FeMn/ZnO samples for 4- and 24 h. After both time points, no significant change ($p > 0.05$) in bacterial viability was observed between the FeMn/ZnO specimens and the control FeMn (Fig. 10A).

The live and dead biovolume of *S. aureus* biofilms adhered to the surface were measured by CLSM and quantified using BiofilmQ. After 4 h no differences between the FeMn control and the FeMn/ZnO groups were identified regarding total biovolume or biofilm thickness of both live and dead *S. aureus* cells (Fig. 10B, C). Similarly, after 24 h no significant differences between the two materials were observed regarding the thickness of biofilms composed of live or dead bacterial cells, or the biovolume of dead cells (Fig. 10B, C). However, after 24 h a significant reduction in live biofilm biovolume was observed on the FeMn/ZnO surface when compared to the FeMn surface (Fig. 10B). Further, while an increase in live *S. aureus* biovolume over time was found in both groups, the fold increase in biovolume of live bacteria between 4- and 24 h was noticeably greater on the control FeMn (9.5-fold increase) than on the FeMn/ZnO coated specimen (4.3-fold increase). Moreover, on the FeMn control, an increase in the dead biovolume of biofilms was also observed over time. In addition, after 24 h of growth, significantly more live *S. aureus* cells than dead were found on the FeMn surface, whereas no difference was found between the live/dead cell proportions on the FeMn/ZnO surface (Fig. 10B). Representative CLSM images of *S. aureus* adhered to the FeMn (Fig. 10D) and the FeMn/ZnO surfaces (Fig. 10E) after 24 h reflect these observations.

The morphology of *S. aureus* biofilms adhered to either the control FeMn or the FeMn/ZnO surface after 24 h incubation was visualised by SEM (Fig. 10F–K). In agreement with the obtained data from CLSM, the total biomass adhered to the FeMn control surface (Fig. 10F–H) was noticeably greater than that adhered to the FeMn/ZnO surface (Fig. 10I–K). *S. aureus* biofilm formed on the FeMn control was thicker and more homogenously distributed across the FeMn surface compared to the FeMn/ZnO surface, where smaller aggregates were common, and the underlying material surface remained visible in many areas. Further, less extracellular polymeric substances (EPS) between bacterial cells were observed on the FeMn/ZnO surface in comparison to the FeMn group (Fig. 10H - red arrows) indicating a less matured and developed biofilm. In combination with this visible reduction in biofilm biomass, more damaged, ruptured and/or dead *S. aureus* cells were observed on the FeMn/ZnO surface (Fig. 10K - blue arrows) when compared to the *S. aureus* cells adhered to the FeMn control.

4. Discussion

4.1. Effect of the ZnO coating on the degradation of FeMn alloys

Several approaches have been tested to increase the corrosion rate of biodegradable iron-based materials, namely, (i) alloying Fe with other elements, such as Mn to shift the corrosion potential towards more negative values and hence, make it more prone to corrosion (ii) introducing porosity to increase the total area susceptible to corrosion attack and, (iii) introducing noble elements that could act as a cathode and cause the formation of micro-galvanic corrosion cells.

In short, the phenomena taking place when a biodegradable metal is in contact with physiological fluids can be described as follows [4,9]: Once the degradable metal is immersed in the fluid, it undergoes an

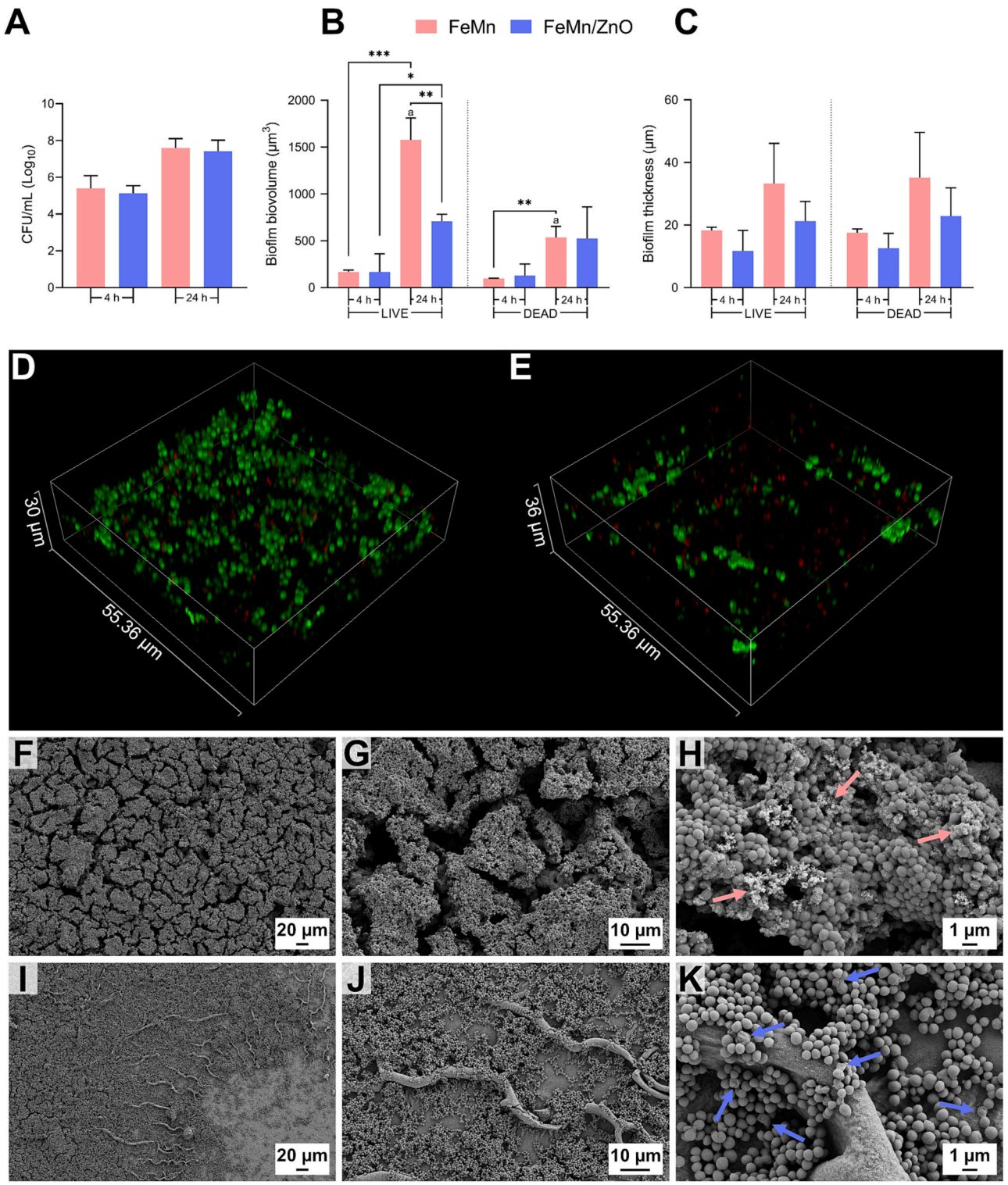

Fig. 10. A) Viable *Staphylococcus aureus* ATCC 25923 adhered to the control FeMn and the ZnO-coated material surfaces after 4 h and 24 h. Quantitative confocal laser-scanning microscopy (CLSM) of *S. aureus* biofilms grown on FeMn/ZnO and FeMn surfaces showing the total B) biofilm biovolume and C) biofilm thickness of live and dead bacteria after 4 h and 24 h. Representative CLSM images of live and dead stained *S. aureus* biofilms grown on the D) FeMn control and the E) FeMn/ZnO coated surfaces for 24 h in which live *S. aureus* cells stain green, and dead stain red. Scanning electron micrographs of *S. aureus* adhered to the surface of the control FeMn (F-H) and FeMn/ZnO (I-K) after 24 h of growth, obtained at increasing magnifications (200×, 1000×, 5000×). Red arrows indicate extracellular polymeric substances (EPS) in the biofilm, whereas blue arrows indicate damaged or dead *S. aureus* cells. (For interpretation of the references to colour in this figure, the reader is referred to the web version of this article.)

oxidation reaction, where metallic ions are released (Eq. (2)). The electrons generated by anodic reaction are consumed during the cathodic reaction, which reduces the amount of dissolved oxygen (Eq. (3)). These reactions occur on the entire metallic surface, and the dissolution of the metal can be accelerated by galvanic coupling between metallic matrix and grain boundaries or secondary phases because of their distinct potentials. Moreover, $M(OH)_n$ corrosion products are deposited on the metal surface (Eq. (4)).

$$M \rightarrow M^{n+} + ne^- \ (anodic\ reaction) \quad (2)$$

$$2H_2O + O_2 + 4e^- \rightarrow 4OH^- (cathodic\ reaction) \quad (3)$$

$$M^{n+} + nOH^- \rightarrow M(OH)_n \ (product\ formation) \quad (4)$$

Physiological solutions such as HBSS contain abundant inorganic ions, which can influence the degradation process by either (i) breaking down the passive film and causing pitting corrosion or (ii) passivating the Fe and slowing down corrosion due to the formation of phosphates and carbonates. Ions such as Cl^- and SO_4^{2-} can break the passive film and accelerate corrosion, while other ions like HPO_4^{2-}/PO_4^{3-}, HCO_3^-/CO_3^{2-} and Ca^{2+} might form a protective layer which further delays degradation of the material [9].

Apart from the reaction between the metal and physiological solution, the structural properties of metals themselves can favour or hinder degradation. The segregation of elements is known for enhancing the corrosion rate of alloys [44]. Two grains of different chemical composition and crystal structure can cause corrosion, for example in the case of duplex steels, which consist of austenite and ferrite grains [43]. This can lead to the formation of galvanic couples between them, where one grain acts as anodic site and the other as cathodic site. This galvanic coupling can lead to the selective dissolution of the less corrosion-resistant grain. Similarly, Donik et al. [19] described that the patterning of FeMn surface by laser ablation leads to the formation of high-temperature oxides, that in turn leads to a shift in the ratio of Fe/Mn to Mn, which ultimately enhances biodegradability of the material. In our study, we observe a similar shift, namely, a difference in the Fe to Fe/Mn ratio around the pores, as well as higher Mn content at the surface due to the oxide formation. The layer just below the surface is enriched in Fe that can also influence corrosion.

The standard corrosion potential of Fe and Mn is −0.44 V and −1.05 V, respectively [39]. When mixed, the potential falls in between (around −0.7 V), with the exact value depending on the alloy composition. In this case, apart from the austenitic FeMn phase, the material consists of ZnO coating, iron-manganese oxide, and the α-Fe phase. This α-Fe phase formed as a side product of iron-manganese oxide formation during annealing, as the particle boundaries adjacent to the oxide layer were depleted in Mn (Figs. 7–8), thus forming an Fe-rich phase. The α-Fe zone at the boundaries causes a difference in potential between the inner regions of the grains and the boundary, thus making the material more prone to corrosion. Moreover, the ZnO and iron-manganese oxide phases can form micro-galvanic cells, leading to an increased corrosion rate, when compared to the non-annealed FeMn. Based on the cross-section images presented in Figs. 7 and 8, we suspect that the FeMn austenite phase (with more negative standard corrosion potential) acts as the anode, while the α-Fe, iron-manganese oxide, and ZnO phases act as the cathode. The pits formed on the cross-sectional area in Fig. 8 indicate that indeed, the austenite matrix may dissolve during the immersion in HBSS. It is important to point out that the pores are not clogged by the ZnO coating and hence the underlying alloy is still exposed to HBSS. The corrosion rate of FeMn/ZnO, presented in Fig. 6, is one order of magnitude higher than corrosion rates given for Fe-based alloys immersed in HBSS under static conditions in the literature while the corrosion rate of FeMn is in accordance with the values found elsewhere [39].

Although previous studies have demonstrated that the deposition of coatings on degradable materials leads to enhanced corrosion resistance, others have reported higher degradation rates when coatings are deposited on Fe-based alloys. The observed increased corrosion was attributed either to the formation of micro-galvanic cells [45] or increased solubility of Fe corrosion products due to polymer hydrolysis when polymeric coatings were deposited [22]. In our case, we attribute the increased corrosion rate of the FeMn/ZnO composite to the segregation of Fe and the formation of micro-galvanic cells between Fe-rich regions and the FeMn matrix, as well as between the ZnO coating and the FeMn underlying material.

4.2. Effect of the accelerated corrosion on the proliferation and cytotoxicity of Saos-2 cells

Indirect cytocompatibility studies using biodegradable Fe-based alloys have been conducted on various types of cells such as fibroblasts [46], smooth muscle cells (SMC) [47] and osteoblasts [46], depending on the target application. Metallic ions released during corrosion may have harmful effects on cellular functions [9]. Hence, it is important to demonstrate that the degradation products being formed during material dissolution are non-toxic to cells. Here, osteoblastic Saos-2 cells were used to investigate the cytocompatibility of the FeMn-based materials.

Experiments were conducted using conditioned media at concentrations of 100 %, 50 %, 25 % and 12.5 %, showing that only the 100 % extract had a cytotoxic effect. The ionic concentrations of Fe and Mn correlate with cell viability. The maximum concentration of released Fe in 100 % extract was 45.3 ± 6.67 mg/L (811 μmol/L), Mn was 57.3 ± 3.2 mg/L (1043 μmol/L), while Zn concentration reached 6.2 ± 0.7 mg/L. Our results obtained are in agreement with previous reports. For instance, it has been reported that Fe concentrations above 50 mg/L can result in decreased metabolic activity [38]. Mueller et al. [47] showed that the SMC growth rate was reduced by the addition of soluble ferrous ions to the cell culture medium. The minimum Mn concentration causing cytotoxic effects depends strongly on the type of cells used [48]; for human lung epithelial cells, a concentration above 20 μmol/L was cytotoxic [49], however, for mouse brain cells, the minimum Mn concentration causing cytotoxicity increased to 200 μmol/L [50] and for HUVEC cells it was even higher, reaching 500 μmol/L [51]. For Saos-2 cells cultured with the 50 % extract, containing Mn concentration of approximately 500 μmol/L, cytotoxicity was not observed. The relatively low release of Zn ions should not cause cytotoxicity, as it is below the threshold value.

While discussing the results of *in vitro* cytocompatibility, we should keep in mind that the tests were performed under static conditions, whereas real *in vivo* conditions are more dynamic [52]. As the cell viability presented in this study clearly depends on the level of dilution, it could be presumed that the concentration of ions and degradation products in a dynamic environment is lower than all the dilutions presented here and, therefore, the material should not cause a cytotoxic effect *in vivo*. For instance, in a study by Loffredo et al. [52], the viability of ECs cells treated with a 1 % eluate concentration of media conditioned with Ag-containing TWIP steels was significantly reduced compared to 316 L stainless steel, while the same materials did not show significant differences in the viability towards SMCs. Therefore, the type of cells used also influences the results of *in vitro* cytocompatibility tests.

In vitro tests of Fe-based degradable alloys are directly affected by the concentration of ions in the culture media [53]. Manganese, iron, and zinc are essential metals found in tissues. The role of Mn is essential for the immune system, bone growth, adjustment of blood sugar, cofactors in enzymes, and others [54]. However, overexposure to Mn can be hazardous in humans, such as Mn-induced neurotoxicity, which occurs in workers exposed to dust-containing Mn. The toxic level of Mn in our case was above 50 ppm. As the concentration of Fe was not significantly different between the samples, the cytotoxicity of 100 % extract could be attributed to the elevated concentration of Mn or to the release of Zn ions. Nevertheless, as the conditions *in vivo* are more dynamic, the

toxicity of 100 % extract should not be of concern when considering the cytocompatibility of FeMn/ZnO, as aforementioned.

4.3. Effect of the accelerated corrosion on S. aureus biofilm formation

Implant-associated infections are an important and debilitating complication of medical implants and have been attributed to the formation of biofilm on the surface of an implant material [24]. A biofilm is a community of bacterial cells irreversibly attached to a substrate and/or each other that are embedded in a self-made matrix of extracellular polymeric substances (polysaccharides, protein, and eDNA) [55]. By adopting a biofilm phenotype, bacterial cells become significantly more resistant to external environmental stresses and challenges, including those from the host-immune system and antibiotic chemotherapy [56]. The stages of bacterial adhesion and biofilm formation are the following: (a) bacterial adhesion, (b) formation of microcolonies, (c) biofilm maturation and (d) biofilm dispersal [26,57]. Many strategies are currently under investigation to avoid or limit the formation of biofilm on the surface of metallic implants such as the incorporation of antibacterial agents such as silver, zinc oxide, *etc*.

Previous research has established that degradable alloys possess better infection resistance than non-degradable ones [25]. One of the potential reasons for their antibacterial/antibiofilm properties can be associated with the effect of degradation on bacterial adhesion [26,58]. This degradation reduces the area available for initial bacterial attachment and colonization and could therefore limit the progression of biofilm formation. Hence, degradable materials with higher corrosion rates should be more resistant to biofilm formation than those with lower corrosion rates. In previous studies on degradable Mg-based alloys, the antibiofilm properties have been associated with an increase in pH and a high release of Mg ions upon degradation [58]. Local pH changes at the material surface were found to limit bacterial attachment. Moreover, bacteria attach preferably to corrosion products and avoid active corrosion sites. In our previous study, Ag-containing Fe-Mn alloys showed an antibiofilm effect higher than in Ag-free Fe-Mn alloys, which could be associated with enhanced corrosion of the former [15]. In this study, a similar effect was observed, as the increased corrosion rate of FeMn/ZnO reduced or delayed the development of biofilm formation more effectively than the slowly corroding uncoated FeMn.

Our results provide more evidence supporting the correlation between enhanced degradation and antibiofilm behaviour. The FeMn/ZnO composite, possessing a higher corrosion rate, has a more pronounced antibiofilm effect than the FeMn sample. As the FeMn/ZnO ion release did not show a bactericidal effect *per se*, the observed antibiofilm properties of FeMn/ZnO may be attributed to the enhanced degradation. It is possible, that the enhanced release of Fe and Mn ions, thus enhanced degradation, limit bacterial attachment and biofilm formation.

5. Conclusions

The main goal of the current study was to determine the effect of sol-gel-derived ZnO coating on porous, equiatomic FeMn alloys on the biodegradability, antibacterial/antibiofilm, and cytocompatibility properties. This study demonstrated that ZnO coating on FeMn leads to increased biodegradation in physiological fluids, making the resulting composite a promising candidate for a biodegradable implant. The results showed that annealing applied to convert the ZnO precursors into ZnO film led to the concomitant formation of secondary phases such as iron-manganese oxide and α-Fe. These secondary phases play a major role in increasing the biodegradability of the FeMn/ZnO samples compared with their uncoated FeMn counterparts. The corrosion rate of FeMn/ZnO, calculated based on ion release, was 36 times higher than that of the uncoated FeMn. Furthermore, FeMn/ZnO showed good cytocompatibility when Saos-2 cells were exposed to diluted conditioned media, for dilutions equal to and below 50 %. The effect of dilution on cytotoxicity strongly correlated with the concentrations of Fe and Mn ions. Moreover, a significant reduction in the total biofilm biovolume of *S. aureus* was observed at 24 h, indicating antibiofilm properties of the FeMn/ZnO sample. In conclusion, FeMn/ZnO possesses better degradability, and is more resistant to biofilm formation than uncoated FeMn, while maintaining good cytocompatibility.

CRediT authorship contribution statement

Aleksandra Bartkowska: Visualization, Investigation, Formal analysis, Writing – original draft. **Adam Benedict Turner:** Visualization, Investigation, Formal analysis. **Andreu Blanquer:** Methodology, Validation, Writing – review & editing, Supervision. **Aliona Nicolenco:** Investigation. **Margarita Trobos:** Methodology, Resources, Writing – review & editing. **Carme Nogues:** Conceptualization, Resources, Supervision. **Eva Pellicer:** Conceptualization, Writing – review & editing, Supervision. **Jordi Sort:** Conceptualization, Resources, Writing – review & editing, Supervision, Funding acquisition.

Declaration of competing interest

There is nothing to disclose.

There were no financial or personal relationships with other people or organizations that could inappropriately influence our work.

AI and AI-assisted technologies were not used in the writing process.

Data availability

Data will be made available on request.

Acknowledgments

This project has received funding from the European Union's Horizon 2020 research and innovation programme under the Marie Skłodowska-Curie grant agreement No. 861046 ('Bioremia' European Training Network), from the Spanish Government (grants PID2020-116844RB-C21 and PID2020 116844RB-C22), from the Generalitat de Catalunya (2021-SGR-00651 and 2021-SGR-00122), from the Swedish Research Council (2022-00853), the Swedish state under the agreement between the Swedish government and the country councils, the ALF-agreement (ALFGBG-978896), and the Hjalmar Svensson Foundation.

Appendix A. Supplementary data

Supplementary data to this article can be found online at https://doi.org/10.1016/j.surfcoat.2023.129886.

References

[1] H. Hermawan, Updates on the research and development of absorbable metals for biomedical applications, Prog. Biomater. 7 (2018) 93–110, https://doi.org/10.1007/s40204-018-0091-4.
[2] H. Hermawan, D. Dubé, D. Mantovani, Developments in metallic biodegradable stents, Acta Biomater. 6 (2010) 1693–1697, https://doi.org/10.1016/j.actbio.2009.10.006.
[3] H. Hermawan, D. Dubé, D. Mantovani, Degradable metallic biomaterials: design and development of Fe-Mn alloys for stents, J. Biomed. Mater. Res. A 93 (2010) 1–11, https://doi.org/10.1002/jbm.a.32224.
[4] H. Hermawan, A. Purnama, D. Dube, J. Couet, D. Mantovani, Fe-Mn alloys for metallic biodegradable stents: degradation and cell viability studies, Acta Biomater. 6 (2010) 1852–1860, https://doi.org/10.1016/j.actbio.2009.11.025.
[5] A.H.M. Yusop, N.M. Daud, H. Nur, M.R.A. Kadir, H. Hermawan, Controlling the degradation kinetics of porous iron by poly(lactic-co-glycolic acid) infiltration for use as temporary medical implants, Sci. Rep. 5 (2015) 11194, https://doi.org/10.1038/SREP11194.
[6] A.H. Yusop, A.A. Bakir, N.A. Shaharom, M.R. Abdul Kadir, H. Hermawan, Porous biodegradable metals for hard tissue scaffolds: a review, Int. J. Biomater. 2012 (2012), 641430, https://doi.org/10.1155/2012/641430.
[7] M.F. Ulum, A. Arafat, D. Noviana, A.H. Yusop, A.K. Nasution, M.R. Abdul Kadir, H. Hermawan, In vitro and in vivo degradation evaluation of novel iron-bioceramic composites for bone implant applications, Mater. Sci. Eng. C 36 (2014) 336–344, https://doi.org/10.1016/j.msec.2013.12.022.

[8] Y. Liu, Y. Zheng, X.-H. Chen, J.-A. Yang, H. Pan, D. Chen, L. Wang, J. Zhang, D. Zhu, S. Wu, K.W.K. Yeung, R.-C. Zeng, Y. Han, S. Guan, Fundamental theory of biodegradable metals—definition, criteria, and design, Adv. Funct. Mater. 29 (2019) 1805402, https://doi.org/10.1002/adfm.201805402.
[9] Y.F. Zheng, X.N. Gu, F. Witte, Biodegradable metals, Mater. Sci. Eng.: R: Rep. 77 (2014) 1–34, https://doi.org/10.1016/j.mser.2014.01.001.
[10] J. Venezuela, M.S. Dargusch, Addressing the slow corrosion rate of biodegradable Fe-Mn: current approaches and future trends, Curr. Opin. Solid State Mater. Sci. 24 (2020), 100822, https://doi.org/10.1016/j.cossms.2020.100822.
[11] H. Hermawan, H. Alamdari, D. Mantovani, D. Dubé, Iron-manganese: new class of metallic degradable biomaterials prepared by powder metallurgy, Powder Metall. 51 (2008) 38–45, https://doi.org/10.1179/174329008X284868.
[12] F. Moszner, A.S. Sologubenko, M. Schinhammer, C. Lerchbacher, A.C. Hänzi, H. Leitner, P.J. Uggowitzer, J.F. Löffler, Precipitation hardening of biodegradable Fe-Mn-Pd alloys, Acta Mater. 59 (2011) 981–991, https://doi.org/10.1016/j.actamat.2010.10.025.
[13] P. Sotoudehbagha, S. Sheibani, M. Khakbiz, S. Ebrahimi-Barough, H. Hermawan, Novel antibacterial biodegradable Fe-Mn-Ag alloys produced by mechanical alloying, Mater. Sci. Eng. C 88 (2018) 88–94, https://doi.org/10.1016/j.msec.2018.03.005.
[14] Z. Ma, M. Gao, D. Na, Y. Li, L. Tan, K. Yang, Study on a biodegradable antibacterial Fe-Mn-C-Cu alloy as urinary implant material, Mater. Sci. Eng. C 103 (2019), 109718, https://doi.org/10.1016/j.msec.2019.05.003.
[15] A. Bartkowska, O. Careta, A.B. Turner, A. Blanquer, E. Ibañez, M. Trobos, C. Nogués, E. Pellicer, J. Sort, Biodegradable porous FeMn(–xAg) alloys: assessment of cytocompatibility, mechanical, magnetic and antibiofilm properties, Mater. Adv. 4 (2023) 616–630, https://doi.org/10.1039/D2MA00867J.
[16] Q. Zhang, P. Cao, Degradable porous Fe-35wt.%Mn produced via powder sintering from NH_4HCO_3 porogen, Mater. Chem. Phys. 163 (2015) 394–401, https://doi.org/10.1016/J.MATCHEMPHYS.2015.07.056.
[17] M. Heiden, E. Nauman, L. Stanciu, Bioresorbable Fe-Mn and Fe-Mn-HA materials for orthopedic implantation: enhancing degradation through porosity control, Adv. Healthc. Mater. 6 (2017) 1700120, https://doi.org/10.1002/adhm.201700120.
[18] T. Huang, Y. Zheng, Y. Han, Accelerating degradation rate of pure iron by zinc ion implantation, Regen. Biomater. 3 (2016) 205–215, https://doi.org/10.1093/rb/rbw020.
[19] Č. Donik, A. Kocijan, I. Paulin, M. Hočevar, P. Gregorčič, M. Godec, Improved biodegradability of Fe–Mn alloy after modification of surface chemistry and topography by a laser ablation, Appl. Surf. Sci. 453 (2018) 383–393, https://doi.org/10.1016/J.APSUSC.2018.05.066.
[20] R. Oriňaková, R. Gorejová, J. Macko, A. Oriňak, M. Kupková, M. Hrubovčáková, J. Ševc, R.M. Smith, Evaluation of in vitro biocompatibility of open cell iron structures with PEG coating, Appl. Surf. Sci. 475 (2019) 515–518, https://doi.org/10.1016/j.apsusc.2019.01.010.
[21] L. Haverová, R. Oriňaková, A. Oriňak, R. Gorejová, M. Baláž, P. Vanýsek, M. Kupková, M. Hrubovčáková, P. Mudroň, J. Radoňák, Z.O. Králová, A. M. Turoňová, An in vitro corrosion study of open cell Iron structures with PEG coating for bone replacement applications, Metals 8 (2018) 499, https://doi.org/10.3390/met8070499.
[22] Y. Qi, X. Li, Y. He, D. Zhang, J. Ding, Mechanism of acceleration of iron corrosion by a polylactide coating, ACS Appl. Mater. Interfaces 11 (2019) 202–218, https://doi.org/10.1021/acsami.8b17125.
[23] S. Huang, A. Ulloa, E. Nauman, L. Stanciu, Collagen coating effects on Fe–Mn bioresorbable alloys, J. Orthop. Res. 38 (2020) 523–535, https://doi.org/10.1002/jor.24492.
[24] H.J. Busscher, H.C. van der Mei, G. Subbiahdoss, P.C. Jutte, J.J.A.M. van den Dungen, S.A.J. Zaat, M.J. Schultz, D.W. Grainger, Biomaterial-associated infection: locating the finish line in the race for the surface, Sci. Transl. Med. 4 (2012) 153rv10, https://doi.org/10.1126/SCITRANSLMED.3004528.
[25] S. Daghighi, J. Sjollema, H.C. van der Mei, H.J. Busscher, E.T.J. Rochford, Infection resistance of degradable versus non-degradable biomaterials: an assessment of the potential mechanisms, Biomaterials 34 (2013) 8013–8017, https://doi.org/10.1016/J.BIOMATERIALS.2013.07.044.
[26] E. Zhang, X. Zhao, J. Hu, R. Wang, S. Fu, G. Qin, Antibacterial metals and alloys for potential biomedical implants, Bioact. Mater. 6 (2021) 2569–2612, https://doi.org/10.1016/J.BIOACTMAT.2021.01.030.
[27] M.L. Kääriäinen, C.K. Weiss, S. Ritz, S. Pütz, D.C. Cameron, V. Mailänder, K. Landfester, Zinc release from atomic layer deposited zinc oxide thin films and its antibacterial effect on Escherichia coli, Appl. Surf. Sci. 287 (2013) 375–380, https://doi.org/10.1016/J.APSUSC.2013.09.162.
[28] K. Thongsuriwong, P. Amornpitoksuk, S. Suwanboon, Structure, morphology, photocatalytic and antibacterial activities of ZnO thin films prepared by sol–gel dip-coating method, Adv. Powder Technol. 24 (2013) 275–280, https://doi.org/10.1016/J.APT.2012.07.002.
[29] L.C. Ann, S. Mahmud, S.K.M. Bakhori, A. Sirelkhatim, D. Mohamad, H. Hasan, A. Seeni, R.A. Rahman, Antibacterial responses of zinc oxide structures against Staphylococcus aureus, Pseudomonas aeruginosa and Streptococcus pyogenes, Ceram. Int. 40 (2014) 2993–3001, https://doi.org/10.1016/J.CERAMINT.2013.10.008.
[30] A. Abdelghafar, N. Yousef, M. Askoura, Zinc oxide nanoparticles reduce biofilm formation, synergize antibiotics action and attenuate Staphylococcus aureus virulence in host; an important message to clinicians, BMC Microbiol. 22 (2022) 244, https://doi.org/10.1186/S12866-022-02658-Z.
[31] S. Stoleriu, C. Lungu, C.D. Ghitulica, A. Surdu, G. Voicu, A. Cucuruz, C.S. Turculet, L.T. Ciocan, Influence of dopant nature on biological properties of ZnO thin-film coatings on Ti alloy substrate, Nanomaterials 10 (2020) 129, https://doi.org/10.3390/NANO10010129.
[32] D. Kim, J.-Y. Leem, Crystallization of ZnO thin films via thermal dissipation annealing method for high-performance UV photodetector with ultrahigh response speed, Sci. Rep. 11 (2021) 382, https://doi.org/10.1038/s41598-020-79849-z.
[33] L. Znaidi, G.J.A.A. Soler Illia, S. Benyahia, C. Sanchez, A.V. Kanaev, Oriented ZnO thin films synthesis by sol–gel process for laser application, Thin Solid Films 428 (2003) 257–262, https://doi.org/10.1016/S0040-6090(02)01219-1.
[34] S.H. Sabeeh, R.H. Jassam, The effect of annealing temperature and Al dopant on characterization of ZnO thin films prepared by sol-gel method, Results Phys. 10 (2018) 212–216, https://doi.org/10.1016/J.RINP.2018.05.033.
[35] L. Znaidi, Sol–gel-deposited ZnO thin films: a review, Mater. Sci. Eng. B 174 (2010) 18–30, https://doi.org/10.1016/J.MSEB.2010.07.001.
[36] Y. Guo, S. Jia, L. Qiao, Y. Su, R. Gu, G. Li, J. Lian, A multifunctional polypyrrole/zinc oxide composite coating on biodegradable magnesium alloys for orthopedic implants, Colloids Surf. B Biointerfaces 194 (2020), 111186, https://doi.org/10.1016/J.COLSURFB.2020.111186.
[37] N. Eliaz, Corrosion of metallic biomaterials: a review, Materials 12 (2019) 407, https://doi.org/10.3390/MA12030407.
[38] S. Zhu, N. Huang, L. Xu, Y. Zhang, H. Liu, H. Sun, Y. Leng, Biocompatibility of pure iron: in vitro assessment of degradation kinetics and cytotoxicity on endothelial cells, Mater. Sci. Eng. C 29 (2009) 1589–1592, https://doi.org/10.1016/J.MSEC.2008.12.019.
[39] B. Liu, Y.F. Zheng, Effects of alloying elements (Mn, Co, Al, W, Sn, B, C and S) on biodegradability and in vitro biocompatibility of pure iron, Acta Biomater. 7 (2011) 1407–1420, https://doi.org/10.1016/J.ACTBIO.2010.11.001.
[40] R. Hartmann, H. Jeckel, E. Jelli, P.K. Singh, S. Vaidya, M. Bayer, D.K.H. Rode, L. Vidakovic, F. Díaz-Pascual, J.C.N. Fong, A. Dragoš, O. Lamprecht, J.G. Thöming, N. Netter, S. Häussler, C.D. Nadell, V. Sourjik, Á.T. Kovács, F.H. Yildiz, K. Drescher, Quantitative image analysis of microbial communities with BiofilmQ, Nat. Microbiol. 6 (2021) 151–156, https://doi.org/10.1038/s41564-020-00817-4.
[41] S.J. Kwon, J.H. Park, J.G. Park, Wrinkling of a sol-gel-derived thin film, Phys. Rev. E Stat. Nonlinear Soft Matter Phys. 71 (2005), 011604, https://doi.org/10.1103/PHYSREVE.71.011604/FIGURES/4/MEDIUM.
[42] T. Kokubo, H. Takadama, How useful is SBF in predicting in vivo bone bioactivity? Biomaterials 27 (2006) 2907–2915, https://doi.org/10.1016/J.BIOMATERIALS.2006.01.017.
[43] J.S. Lee, K. Fushimi, T. Nakanishi, Y. Hasegawa, Y.S. Park, Corrosion behaviour of ferrite and austenite phases on super duplex stainless steel in a modified green-death solution, Corr. Sci. 89 (2014) 111–117, https://doi.org/10.1016/J.CORSCI.2014.08.014.
[44] K.W. Chan, S.C. Tjong, Effect of secondary phase precipitation on the corrosion behavior of duplex stainless steels, Materials 7 (2014) 5268–5304, https://doi.org/10.3390/MA7075268.
[45] J. Cheng, T. Huang, Y.F. Zheng, Relatively uniform and accelerated degradation of pure iron coated with micro-patterned Au disc arrays, Mater. Sci. Eng. C 48 (2015) 679–687, https://doi.org/10.1016/j.msec.2014.12.053.
[46] A. Yamamoto, R. Honma, M. Sumita, Cytotoxicity evaluation of 43 metal salts using murine fibroblasts and osteoblastic cells, J. Biomed. Mater. Res. (1998) 331–340. https://onlinelibrary.wiley.com/doi/epdf/10.1002/%28SICI%291097-4636%28199802%2939%3A2%3C331%3A%3AAID-JBM22%3E3.0.CO%3B2-E.
[47] P.P. Mueller, T. May, A. Perz, H. Hauser, M. Peuster, Control of smooth muscle cell proliferation by ferrous iron, Biomaterials 27 (2006) 2193–2200, https://doi.org/10.1016/J.BIOMATERIALS.2005.10.042.
[48] J. Čapek, J. Kubásek, D. Vojtěch, E. Jablonská, J. Lipov, T. Ruml, Microstructural, mechanical, corrosion and cytotoxicity characterization of the hot forged FeMn30 (wt.%) alloy, Mater. Sci. Eng. C 58 (2016) 900–908, https://doi.org/10.1016/J.MSEC.2015.09.049.
[49] L.E. Pascal, D.M. Tessier, Cytotoxicity of chromium and manganese to lung epithelial cells in vitro, Toxicol. Lett. 147 (2004) 143–151, https://doi.org/10.1016/J.TOXLET.2003.11.004.
[50] N.M. Filipov, R.F. Seegal, D.A. Lawrence, Manganese potentiates in vitro production of proinflammatory cytokines and nitric oxide by microglia through a nuclear factor kappa B–dependent mechanism, Toxicol. Sci. 84 (2005) 139–148, https://doi.org/10.1093/TOXSCI/KFI055.
[51] M. Schinhammer, I. Gerber, A.C. Hänzi, P.J. Uggowitzer, On the cytocompatibility of biodegradable Fe-based alloys, Mater. Sci. Eng. C 33 (2013) 782–789, https://doi.org/10.1016/J.MSEC.2012.11.002.
[52] S. Loffredo, S. Gambaro, F. Copes, C. Paternoster, N. Giguère, M. Vedani, D. Mantovani, Effect of silver in thermal treatments of Fe-Mn-C degradable metals: implications for stent processing, Bioact. Mater. 12 (2022) 30–41, https://doi.org/10.1016/j.bioactmat.2021.10.020.
[53] D.T. Chou, D. Wells, D. Hong, B. Lee, H. Kuhn, P.N. Kumta, Novel processing of iron–manganese alloy-based biomaterials by inkjet 3-D printing, Acta Biomater. 9 (2013) 8593–8603, https://doi.org/10.1016/J.ACTBIO.2013.04.016.
[54] K.M. Erikson, T. Syversen, J.L. Aschner, M. Aschner, Interactions between excessive manganese exposures and dietary iron-deficiency in neurodegeneration, Environ. Toxicol. Pharmacol. 19 (2005) 415–421, https://doi.org/10.1016/J.ETAP.2004.12.053.
[55] R.M. Donlan, J.W. Costerton, Biofilms: survival mechanisms of clinically relevant microorganisms, Clin. Microbiol. Rev. 15 (2002) 167–193, https://doi.org/10.1128/CMR.15.2.167-193.2002.
[56] K. Svensson Malchau, J. Tillander, M. Zaborowska, M. Hoffman, I. Lasa, P. Thomsen, H. Malchau, O. Rolfson, M. Trobos, Biofilm properties in relation to treatment outcome in patients with first-time periprosthetic hip or knee joint

infection, J. Orthop. Translat. 30 (2021) 31–40, https://doi.org/10.1016/j.jot.2021.05.008.
[57] K. Zhang, X. Li, C. Yu, Y. Wang, Promising therapeutic strategies against microbial biofilm challenges, Front. Cell. Infect. Microbiol. 10 (2020) 359, https://doi.org/10.3389/FCIMB.2020.00359.
[58] N. Wang, Y. Ma, H. Shi, Y. Song, S. Guo, S. Yang, Mg-, Zn-, and Fe-based alloys with antibacterial properties as orthopedic implant materials, Front. Bioeng. Biotechnol. 10 (2022) 684, https://doi.org/10.3389/FBIOE.2022.888084.